GEOTECHNICAL ENGINEERING

Laboratory Model Testing and DEM Simulation of Bearing Capacity and Localized Deformation in Uniformly Graded Sand

Mustapha Zakariya'u Lawal[1], Kong Fah Tee[2, 3]

[1]School of Civil Engineering, Beijing Jiaotong University, Beijing, China
[2]Department of Civil and Environmental Engineering, King Fahd University of Petroleum and Minerals, Dhahran, Saudi Arabia
[3]Interdisciplinary Research Center for Construction and Building Materials, King Fahd University of Petroleum and Minerals, Dhahran, Saudi Arabia

Published November 2026

Abstract

Ground bearing capacity and localized deformation beneath shallow foundations remain important problems in geotechnical engineering. This study examines a rigid rectangular footing (70 mm × 50 mm) on dry, uniformly graded sand (d_{50} = 3.0 mm; C_u = 1.3; C_c = 1.0) using a laboratory model test, DIC-assisted imaging, and DEM simulations with single-sphere and four-sphere clumped particles. The selected experimental bearing pressure was 561.00 kPa at 20.62 mm settlement, based on the maximum-curvature criterion, equivalent to 29.5% of the 70-mm footing dimension. Visible deformation zones were estimated to orient at 44.33° and 48.80° on the left and right; these are approximate image-based directions, not theoretical slip-surface angles. The DEM simulations gave ultimate pressures of 445.57 kPa (single sphere) and 527.87 kPa (clump), 20.58% and 5.91% below the experimental value, respectively. Since the two DEM representations were calibrated separately and used different material/contact parameters, the closer clump-model agreement cannot be attributed to particle shape alone and is not an independent validation. The results are model-scale observations affected by the container boundaries and should not be directly extrapolated to full-scale design.

Keywords: bearing capacity; clumped particles; discrete element method; digital image correlation; uniformly graded sand

Nomenclature

Table 1 lists the symbols used in this paper.

Table 1. Nomenclature used in the manuscript.

Symbol	Definition
B	Footing width (m or mm)
c	Soil cohesion (kPa)
C_c	Coefficient of curvature
C_u	Coefficient of uniformity
d_{10}, d_{30}, d_{50}, d_{60}	Characteristic particle diameters (mm)
E	Young's modulus (Pa)
e	Void ratio

Symbol	Definition
G	Shear modulus (Pa)
n	Porosity
q_u	Ultimate ground bearing capacity (kPa)
s or U_y	Footing settlement or vertical displacement (mm)
γ	Unit weight (kN/m^3)
γ_{xy}	Engineering shear strain
θ	Localized deformation orientation angle
φ	Angle of internal friction

Introduction

Shallow foundations are widely used to transfer structural loads to the supporting ground. Their safety and serviceability depend on the ability of the underlying soil to resist excessive settlement and shear failure. For coarse-grained soils, this response is governed not only by macroscopic strength parameters but also by particle rearrangement, interlocking, rolling resistance, and the development of localized deformation [1, 2]. A reliable interpretation of shallow foundation behavior therefore requires both the load-settlement response and the internal deformation mechanism to be examined together.

Classical bearing capacity theories provide important analytical foundations for geotechnical design. Terzaghi's formulation and the later extensions by Meyerhof, Hansen, and Vesic remain essential references for interpreting shallow foundation failure and preliminary bearing-capacity estimation [3]. These theories are valuable because they provide simple and physically meaningful relationships between soil strength, footing geometry, and bearing resistance. However, they generally idealize soil as a continuum and assume simplified failure surfaces. Such assumptions can be difficult to satisfy in model-scale tests on coarse-grained soil, particularly when the footing size is small relative to the particle size and when the model box creates boundary confinement.

Laboratory model testing provides a controlled way to observe the progressive response of soil under footing loading [4]. Conventional load and settlement measurements are useful for determining stiffness and ultimate capacity, but they cannot fully describe the spatial distribution of deformation. Digital Image Correlation (DIC) has become a useful non-contact measurement technique in geotechnical model testing because it can provide displacement and strain fields from images recorded during loading [5, 6]. In this study, DIC is used strictly as a measurement and post-processing tool for interpreting physical model tests. It is not treated as an independent failure theory. The Discrete Element Method (DEM) provides a complementary particle-scale tool for studying granular soil behavior. Since the method represents soil as an assembly of interacting particles, it can reveal particle displacement, contact force chains, and deformation mechanisms that are not directly measured in the experiment [7, 8]. DEM simulations of coarse-grained soils are, however, highly sensitive to particle representation and contact parameters [9–12]. The use of simple spherical particles can reduce computational cost but may underestimate angularity, interlocking, and rolling resistance. Clumped particles can better represent irregular particle shape, but they also require careful calibration and interpretation.

The present study addresses this problem through a combined laboratory model test and calibrated DEM simulation of a shallow footing on dry uniformly graded coarse-grained soil. The novelty of the work lies in the direct comparison of experimental bearing response with two DEM particle representations under the same model geometry, together with a careful interpretation of DIC-assisted deformation fields, force-chain development, and boundary effects. The study is deliberately framed as a model-scale investigation: the measured bearing capacity and deformation pattern are used to explain mechanisms and compare DEM particle models, not to provide direct full-scale design values.

The objectives of this paper are to: (i) determine the load-settlement response and ultimate ground bearing capacity of the tested dry uniformly graded coarse-grained soil; (ii) use DIC-assisted measurement to observe displacement and shear strain fields during footing loading; (iii) estimate visible localized deformation orientation using the manual visual line method; (iv) compare single-sphere and 4-sphere clumped-particle DEM models; and (v) interpret the results considering particle-shape effects, force-chain development, boundary confinement, and model-scale limitations.

Materials and methods

Test material and model geometry

The tested material was a dry uniformly graded sandy coarse-grained soil. The material had a median particle size of d_{50} = 3.0 mm, coefficient of uniformity C_u = 1.3, and coefficient of curvature C_c = 1.0. These values indicate a narrow particle-size range and confirm that the material was uniformly graded. The soil was tested under dry conditions; water content, saturation, suction, and seepage effects were not included in the present study.

The physical model comprised a transparent model box (600 mm × 50 mm × 250 mm) and a rigid rectangular steel footing (70 mm × 50 mm × 40 mm; contact area 0.0035 m^2). The soil bed was 250 mm high. The reported dimensions include a 50-mm box dimension and a 50-mm footing plan dimension; the available side clearance is therefore potentially restrictive. The boundary condition is treated as a potential source of confinement, and plane-strain behavior is not assumed.

Table 2 summarizes the material properties and model parameters, and Table 3 gives the particle-size distribution (Figure 1). Figure 2 shows the physical and DEM model geometry.

Table 2. Experimental material properties and model parameters.

Parameter	Value
Soil type	Dry uniformly graded sandy coarse-grained soil
d_{10}	2.64 mm
d_{30}	2.95 mm
d_{50}	3.00 mm
d_{60}	3.30 mm
C_u	1.3
C_c	1.0
Specific gravity, G_s	2.65
Dry density, ρ_d	1.6135 g/cm^3
Void ratio, e	0.642

Parameter	Value
Porosity, n	0.391
Cohesion, c	0 kPa
Internal friction angle, φ	33.3°
Footing dimensions	70 mm × 50 mm × 40 mm
Footing area	0.0035 m^2
Model box width	50 mm
B/d_{50}	23.3

Table 3. Particle size distribution adopted for the uniformly graded coarse-grained soil.

Particle size descriptor	Size (mm)	Percent passing (%)
d_{min}	2.50	0
d_{10}	2.64	10
d_{30}	2.95	30
d_{50}	3.00	50
d_{60}	3.30	60
d_{max}	4.00	100

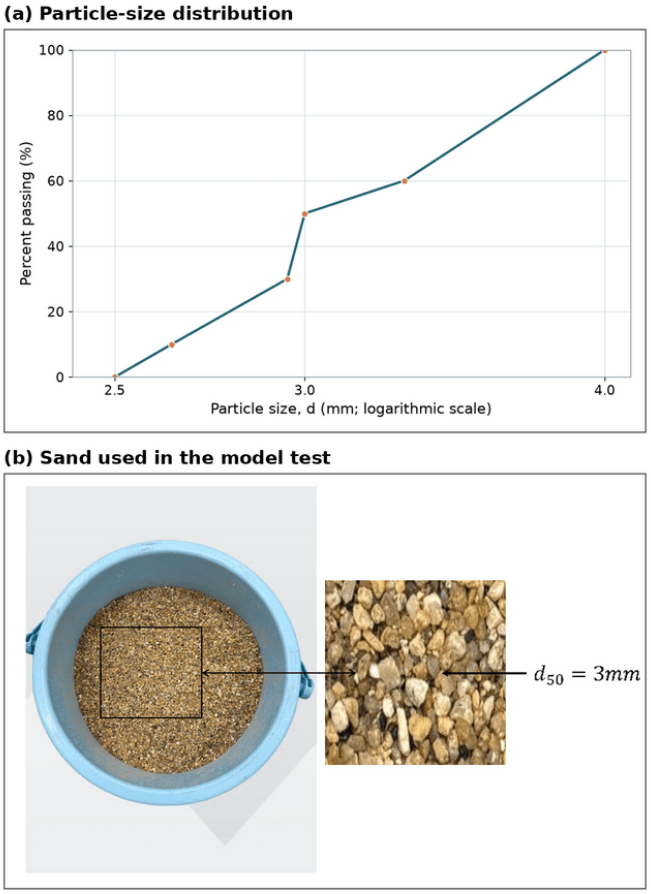


Figure 1. Particle-size distribution curve and photographs of the dry, uniformly graded sand used in the laboratory model test.

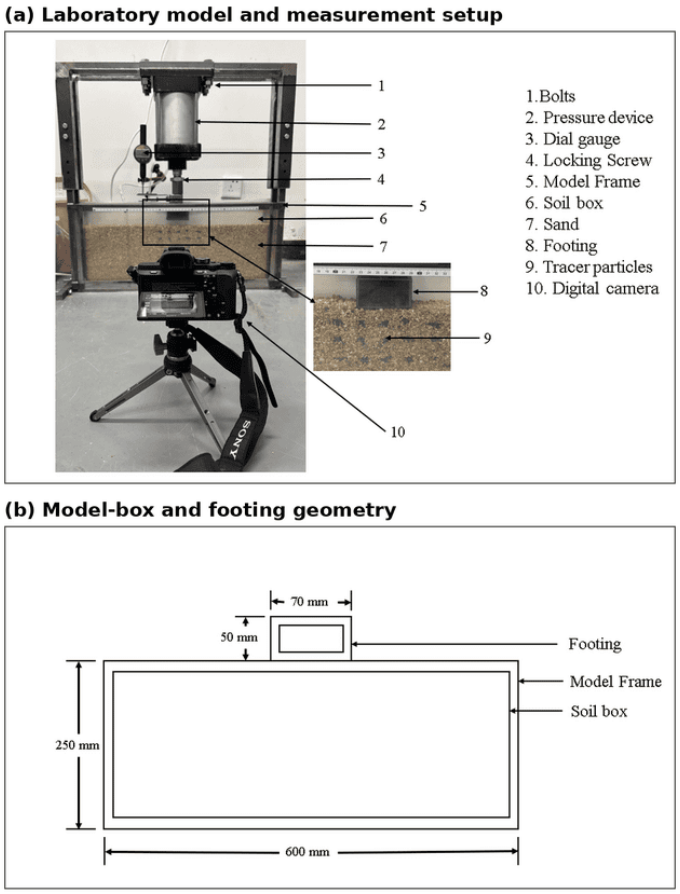


Figure 2. Physical model and DEM geometry: transparent box (600 mm × 50 mm × 250 mm), rigid footing (70 mm × 50 mm × 40 mm), and vertical loading system.

Laboratory test procedure and DIC-assisted measurement

A 24.3-megapixel Sony camera (6000 × 4000 pixels) was positioned approximately 0.5 m from the transparent observation panel. Approximately 1-mm black sand tracers were distributed on the exposed soil face; a 100-mm ruler provided image-scale calibration, and diffused lighting was used to reduce glare. Images were processed using Ncorr and custom MATLAB scripts to obtain displacement and strain fields. A Gaussian filter was applied to the shear-strain data. DIC was used as a measurement and post-processing tool, not as an independent failure theory.

The experimental load–settlement data were smoothed using a 5-point moving average. The ultimate point was selected at the peak of the second-derivative approximation of the smoothed response (maximum-curvature method); bearing pressure was calculated as vertical load divided by the footing contact area. The selected point should be understood as an operational criterion for this test, rather than a uniquely defined full-scale failure capacity.

Figure 3 shows the photographs of the soil face recorded during loading.

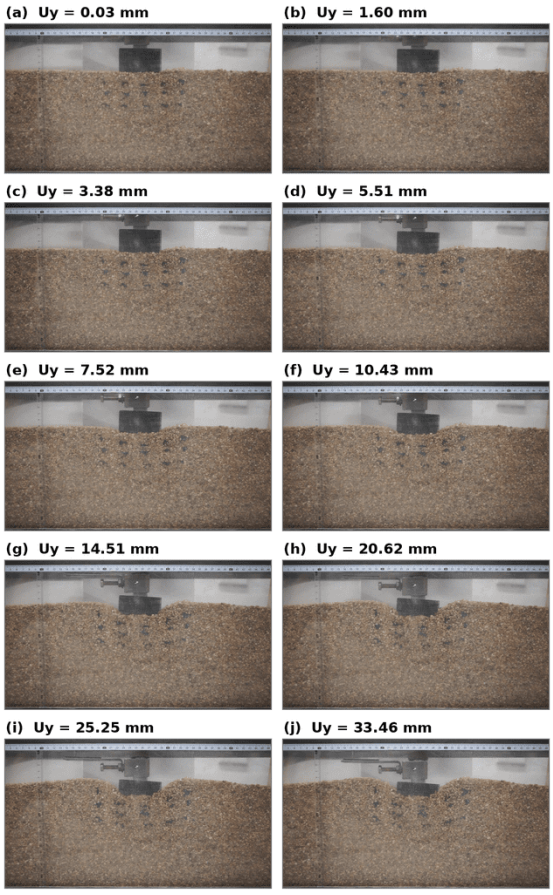


Figure 3. Photographs of the soil surface during loading at footing settlements Uy = 0.03, 1.60, 3.38, 5.51, 7.52, 10.43, 14.51, 20.62, 25.25, and 33.46 mm (panels a–j); these are the source images used for DIC processing.

Manual visual line method for localized deformation orientation

The orientation of the visible localized-deformation zones was estimated using the manual visual line method. Representative lines were drawn along the central direction of the left and right zones, and their angles were measured relative to the horizontal. Two points were selected on each line and the angle calculated as $\theta = \tan^{-1}(\Delta y/\Delta x)$. The zones were diffuse, so the resulting angles are approximate visual orientations, not exact theoretical slip-surface angles.

The measured angles are interpreted as approximate visual orientations of localized deformation, not as exact theoretical slip-surface angles. This distinction is important because the model-scale soil response was affected by diffuse deformation, boundary confinement, local particle arrangement, and footing-to-particle-size ratio.

DEM model setup and particle representation

DEM simulations were conducted using EDEM to reproduce the physical model test geometry. The model box, soil domain, and rigid rectangular footing were created using the same dimensions as the laboratory model. The simulation was three-dimensional because EDEM represents particles and contact interactions in three-dimensional space. Nevertheless, the box boundaries may constrain deformation; geometry alone does not establish plane-strain conditions.

Two particle representations were compared: single spheres and four-sphere clumps. Each clump comprised four identical 3.0-mm spheres in a tetrahedral arrangement; the clumps were treated as rigid particles. Both assemblies used a target void ratio of 0.642 and the same model geometry.

However, material stiffness and soil-soil friction/rolling-friction parameters differed between the separately calibrated models (Tables 4 and 5). Thus, the results compare calibrated configurations and do not isolate particle shape alone.

The rigid footing was loaded by vertical linear translation at a prescribed velocity, while horizontal movement was restricted to maintain loading alignment. Footing rotation was not treated as a principal DEM validation parameter. The numerical comparison focused on vertical reaction force, footing settlement, particle velocity, particle displacement, contact force chains, and deformation pattern.

Figure 4 shows the two particle representations.

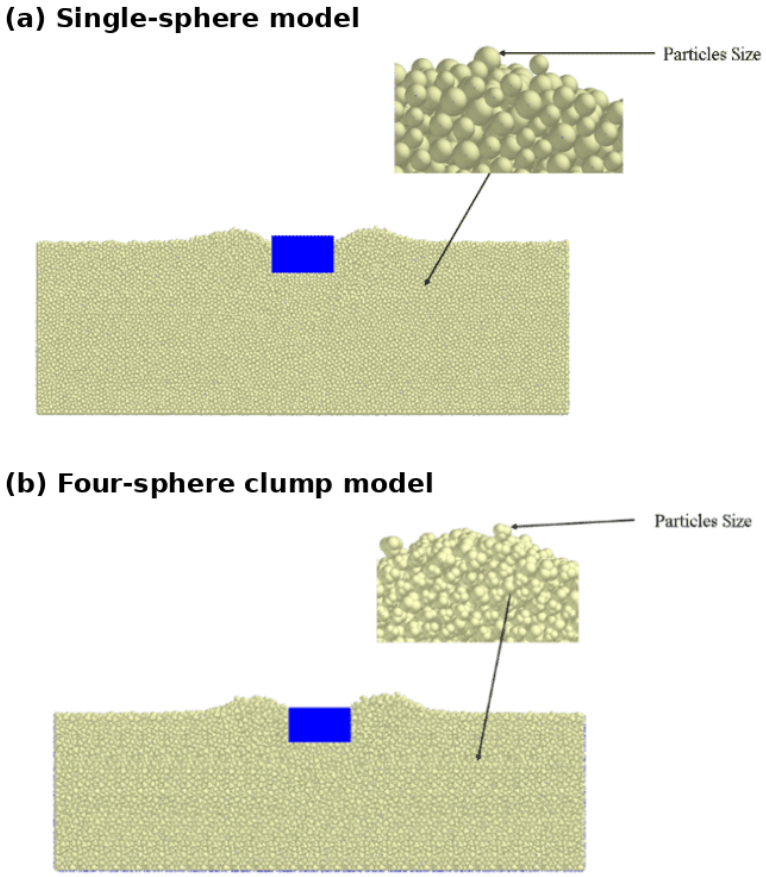


Figure 4. DEM particle representations: (a) single-sphere particles and (b) four-sphere clumps, with the clump spheres arranged tetrahedrally.

DEM calibration and contact parameters

The DEM material and contact parameters were calibrated against the experimental load–settlement response and ultimate capacity. The sphere and clump models were calibrated separately and use different final stiffness and friction/rolling-friction parameters (Tables 4 and 5), so this comparison does not isolate particle shape. Because the experiment informed calibration, the numerical agreement is a calibrated reproduction rather than independent validation. The footing was prescribed at 0.5 mm/min; reaction force, settlement, particle motion, and contact forces were monitored.

Table 4. DEM material parameters used for single-sphere and clumped-particle models.

Model	Material	Density (kg/m³)	Poisson's ratio	Young's modulus (Pa)	Shear modulus (Pa)
Single sphere	Soil	2650	0.25	3.0×10^8	1.2×10^8
Single sphere	Steel	7850	0.25	2.5×10^8	1.0×10^8
Single sphere	Plastic glass	2500	0.25	2.5×10^8	1.0×10^8
Clump	Soil	2650	0.25	3.25×10^8	1.3×10^8
Clump	Steel	7850	0.25	2.5×10^8	1.2×10^8
Clump	Plastic glass	2500	0.25	2.5×10^8	1.0×10^8

Table 5. Calibrated DEM contact parameters used in simulations.

Model	Contact pair	Restitution	Static friction	Rolling friction	Rolling stiffness	Damping ratio
Single sphere	Soil-soil	0.55	0.57	0.25	3	0.3
Single sphere	Soil-steel	0.55	0.75	0.75	3	0.3
Single sphere	Soil-plastic glass	0.55	0.35	0.35	3	0.3
Clump	Soil-soil	0.55	0.66	0.67	3	0.3
Clump	Soil-steel	0.55	0.75	0.75	3	0.3
Clump	Soil-plastic glass	0.55	0.35	0.35	3	0.3

Results and discussion

Load-settlement behavior and ultimate ground bearing capacity

The experimental load-settlement curve (Figure 5) showed a nonlinear response. At the initial loading stage, settlement increased gradually as the particles rearranged beneath the footing. With further loading, the settlement rate increased and the curve developed a sharper bend, indicating transition toward failure-dominated deformation.

Using the stated maximum-curvature procedure, the selected pressure was q_u = 561.00 kPa at a settlement of 20.62 mm. With B defined here as the 70-mm footing dimension, U_y/B = 20.62/70 = 0.2946 (29.5%). This large normalized settlement is specific to the selected operational criterion and model-scale test; it should not be interpreted as a typical design settlement or a directly transferable full-scale failure value.

Table 6 lists the measured load–settlement data.

Table 6. Experimental load–settlement data for the selected coarse-grained soil.

No.	Applied pressure q (kPa)	Settlement U_y (mm)	Normalized settlement U_y/B
1	70.125	0.03	0.0004
2	192.843	1.60	0.0229
3	280.499	3.38	0.0483
4	368.155	5.51	0.0787
5	420.749	7.52	0.1074

No.	Applied pressure q (kPa)	Settlement U_y (mm)	Normalized settlement U_y/B
6	473.343	10.43	0.1490
7	525.936	14.51	0.2073
8	560.999	20.62	0.2946
9	578.530	25.25	0.3607
10	648.655	26.52	0.3789
11	718.780	33.46	0.4780

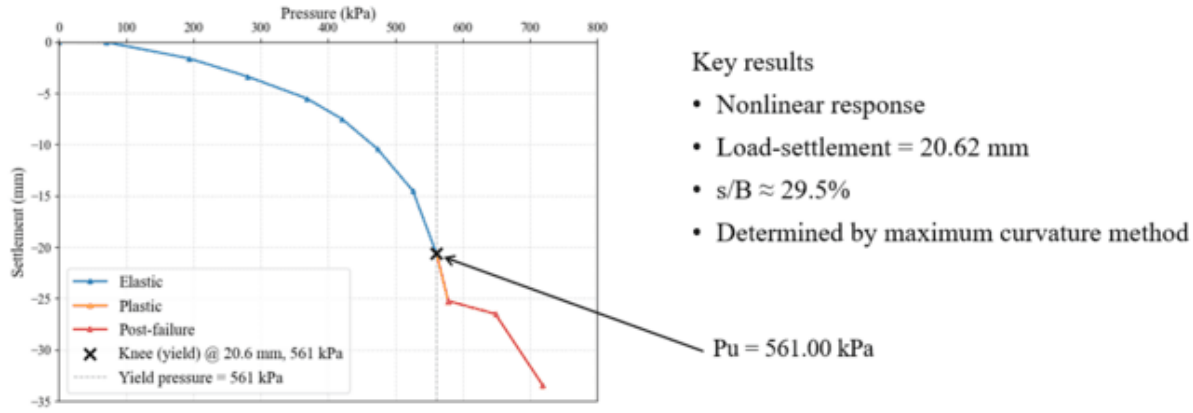


Figure 5. Experimental bearing-pressure-settlement response. The marked point is the 561.00-kPa maximum-curvature estimate at Uy = 20.62 mm; pressure is normalized by the 0.0035-m^2 footing area.

DIC-assisted displacement and shear strain fields

The photographs in Figure 3 show progressive footing settlement. The DIC-derived vertical-displacement field at the selected maximum-curvature stage is shown in Figure 6. The shear-strain fields in Figure 7 show initially diffuse deformation followed by increasingly localized zones near the footing edges. The deformation remained diffuse overall, and idealized Terzaghi failure zones were not clearly separated; the observed pattern is therefore described as localized shear deformation with a general-shear tendency.

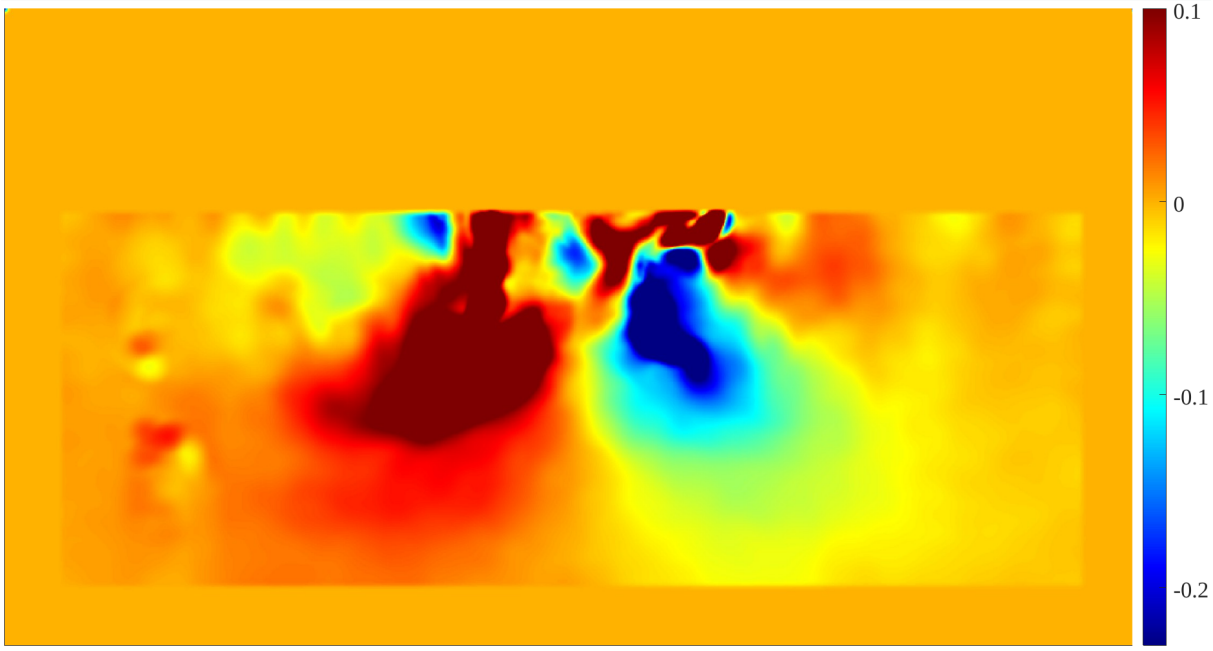


Figure 6. DIC-derived vertical-displacement field at the selected maximum-curvature stage (Uy = 20.62 mm). The color scale reports vertical displacement in millimetres.

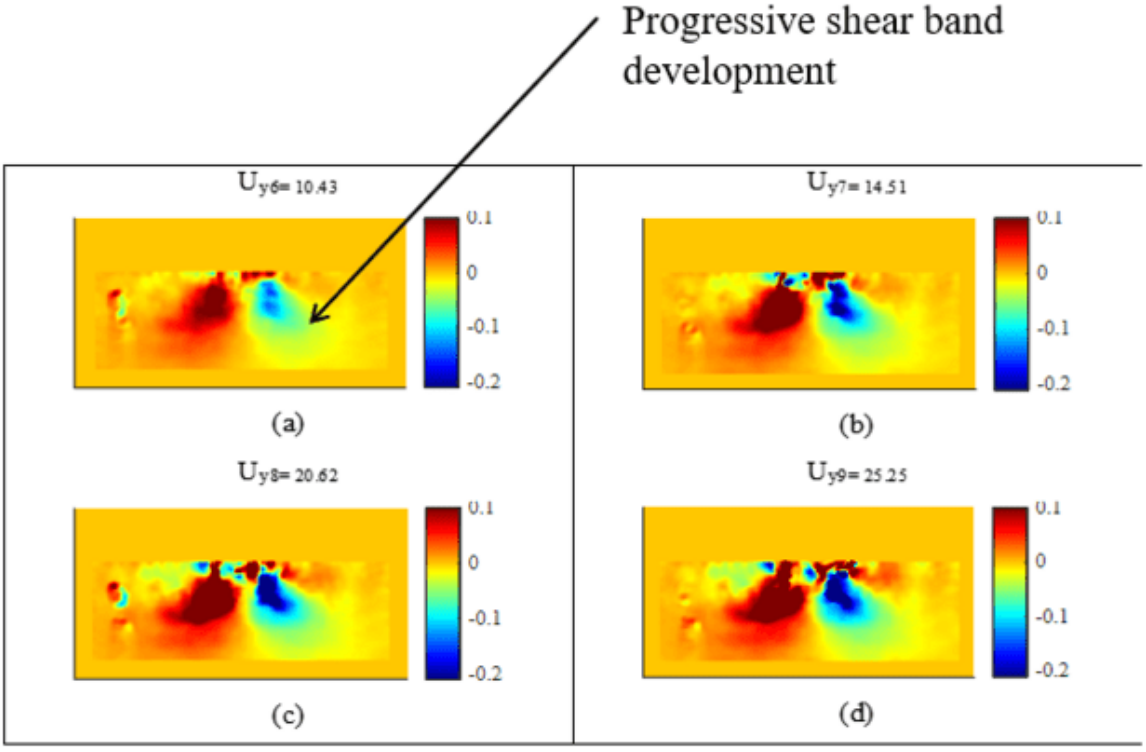


Figure 7. DIC-derived shear-strain field γxy at Uy = 10.43, 14.51, 20.62, and 25.25 mm (panels a–d), showing progressive localization near the footing edges; the same color scale is used across panels.

Localized deformation orientation

The manual visual line method was used to estimate the orientations of the visible localized-deformation zones (Figure 8). The measured left-side angle was 44.33°, and the right-side angle was 48.80°, both measured relative to the horizontal. Their arithmetic mean is 46.565° (46.57° to two decimal places). These are approximate image-based orientations, not theoretical slip-surface angles.

The manual line method is subjective because the selected points depend on the visible extent of the diffuse zones. The small left–right angle difference is therefore descriptive only and should not be interpreted as significant asymmetry.

Table 7 summarizes the measured orientations.

Table 7. Localized deformation orientation measured using the manual visual line method.

Measurement	Angle (°)	Interpretation
Left localized deformation zone	44.33	Manual visual line measurement
Right localized deformation zone	48.80	Manual visual line measurement
Average orientation	46.57	Representative visual orientation

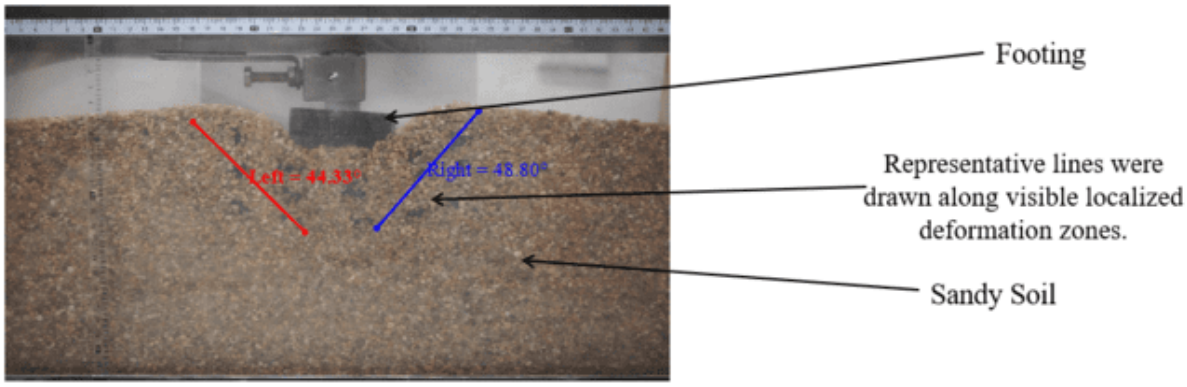


Figure 8. Manual visual measurement of localized-deformation orientation: representative lines on the left and right sides give 44.33° and 48.80°, measured relative to the horizontal.

DEM particle movement and force-chain development

The DEM particle-velocity fields (Figure 9, top row) show downward movement beneath the footing and outward movement near its edges, qualitatively consistent with the experimental settlement and lateral movement. The two models exhibit different movement patterns; these are qualitative observations from separately calibrated simulations.

The DEM contact-force-chain visualizations (Figure 9, bottom row) show force transmission beneath the footing. Figure 10 presents the corresponding normal-contact-force magnitude maps in newtons. These visualizations support a particle-scale interpretation, but no quantitative force-chain metric was calculated; they do not by themselves establish why one calibrated model matched the test more closely.

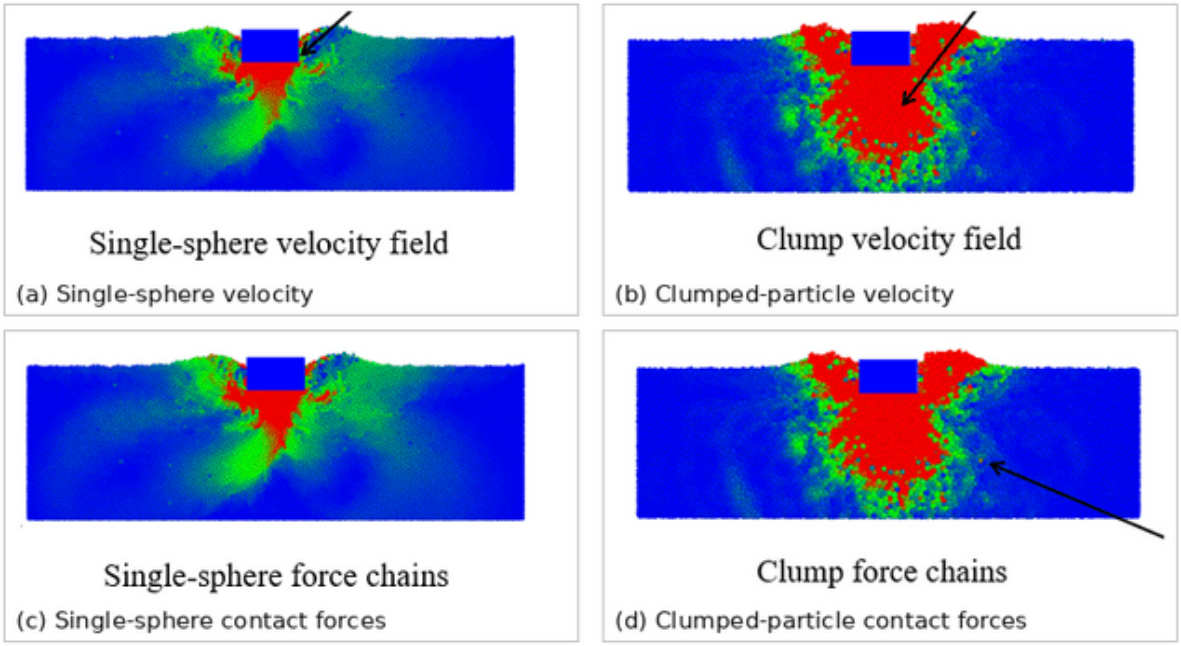


Figure 9. DEM fields for the single-sphere and clumped-particle models: particle velocity in the top row and contact-force patterns in the bottom row; columns compare the two particle representations.

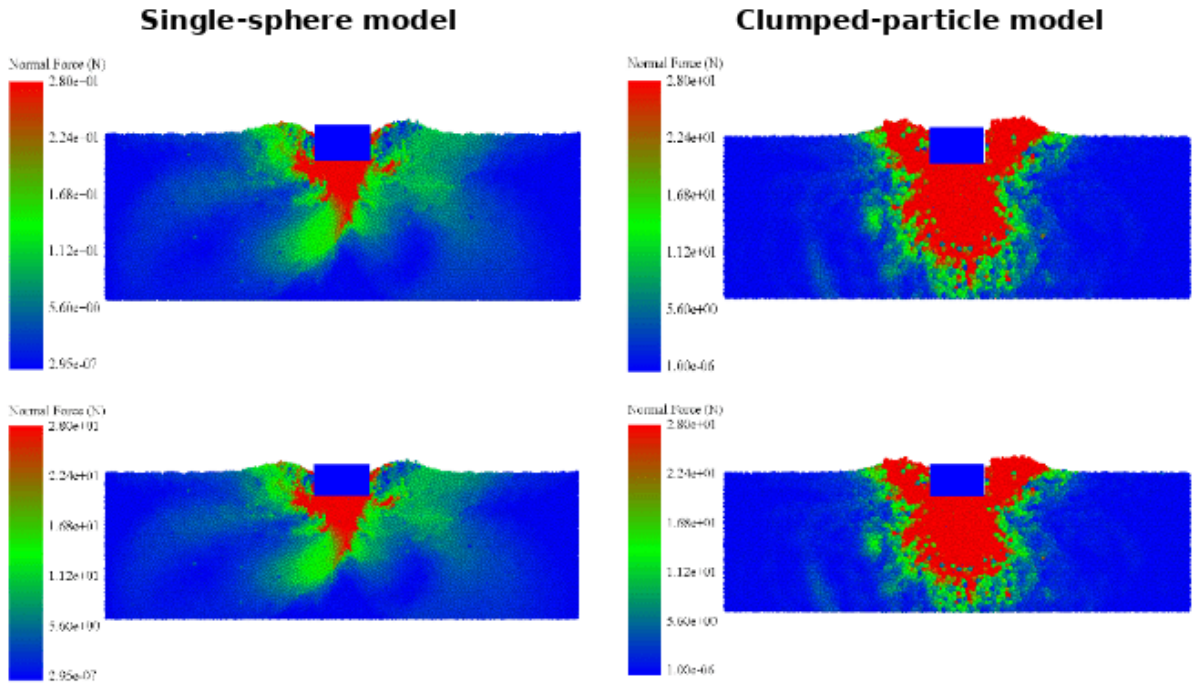


Figure 10. DEM normal-contact-force magnitude maps (N) beneath the footing. The left column shows the single-sphere model and the right column the clumped-particle model; color bars denote normal force.

DEM-experiment comparison of calibrated particle representations

The DEM-experiment comparison (Figure 11) shows that both DEM models reproduced the general trend of the experimental load-settlement curve. However, the single-sphere model underestimated the ultimate ground bearing capacity more strongly than the clumped-particle model. The experimental ultimate capacity was 561.00 kPa, while the single-sphere and clumped-particle models predicted 445.57 kPa and 527.87 kPa, respectively.

The absolute percentage differences from the experimental value were 20.58% and 5.91%, respectively. The lower difference for the clump configuration indicates closer agreement for this calibration and test. Because each representation was calibrated separately and other model parameters differ, the difference cannot be attributed to particle shape alone and should not be generalized as proof that shape is the controlling factor.

Table 8 and Figure 12 compare the ultimate bearing capacities.

Table 8. Ultimate ground bearing capacity comparison among physical model test and DEM simulations.

Method	Ultimate bearing capacity q_u (kPa)	Absolute error (kPa)	Percentage error (%)
Physical model test	561.00	—	—
DEM single-sphere model	445.57	115.43	20.58
DEM 4-sphere clumped-particle model	527.87	33.13	5.91

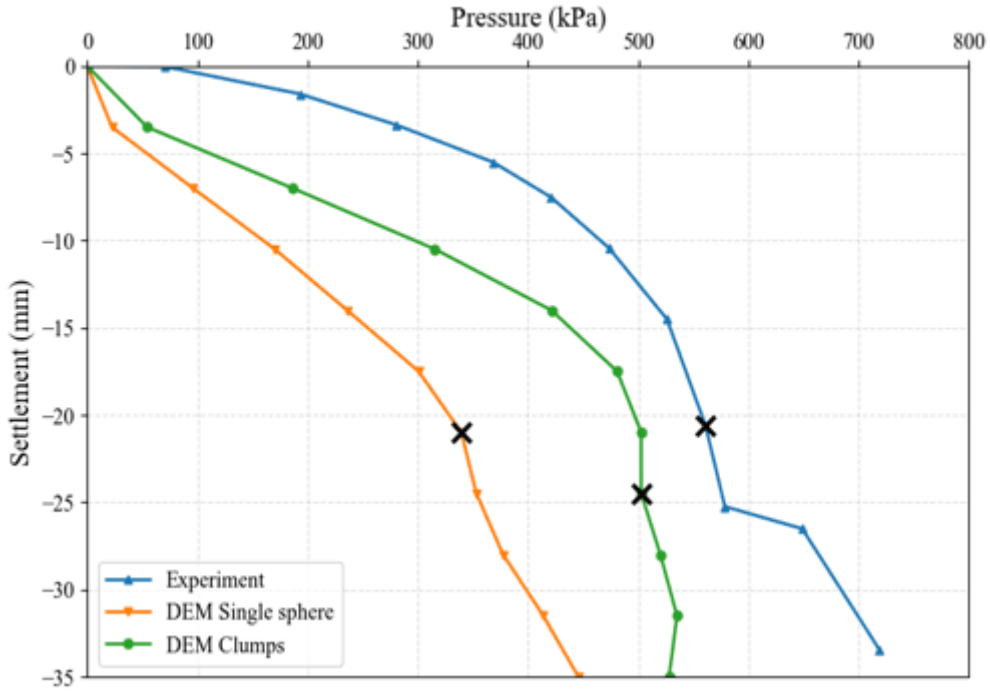


Figure 11. Experimental and DEM pressure-settlement curves. Markers identify the selected maximum-curvature capacities for the physical test and the separately calibrated DEM models.

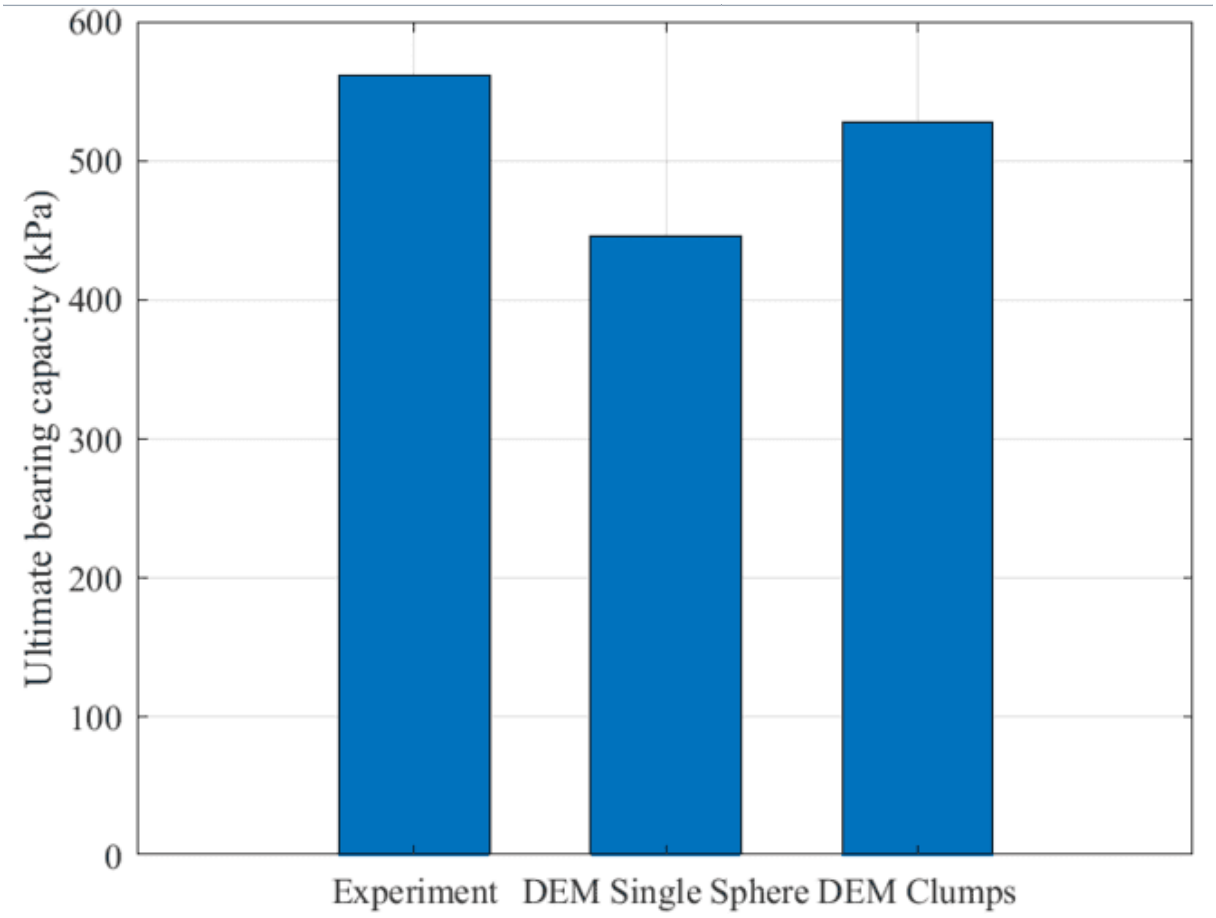


Figure 12. Ultimate bearing capacities: physical test, 561.00 kPa; single-sphere DEM, 445.57 kPa; and clumped-particle DEM, 527.87 kPa. No uncertainty bars are shown because replicate variability was not quantified.

Boundary effect, scale effect, and classical theory interpretation

The model box measured 600 mm × 50 mm × 250 mm, while the footing measured 70 mm × 50 mm × 40 mm. The 50-mm box and footing dimensions imply potentially restrictive side clearance, depending on the footing orientation. The results are therefore interpreted as boundary-affected model-scale observations; plane-strain behavior is not assumed. B/d_{50} = 23.3 uses B = 70 mm.

Classical bearing capacity theory is therefore used in this paper as a qualitative reference rather than as a direct numerical prediction for the confined model-scale test. The observed deformation shows localized shear deformation with a general shear failure tendency, but the idealized Zone I, Zone II, and Zone III regions were not clearly separated. The results should not be directly extrapolated to full-scale foundation design without considering boundary effects, scale effects, and similarity requirements [13, 14].

Conclusion

1. The laboratory test produced a nonlinear load-settlement response. The operational maximum-curvature criterion selected 561.00 kPa at 20.62 mm settlement (29.5% of B, with B = 70 mm); this value is specific to the model test and criterion.
2. DIC-assisted deformation measurement showed settlement concentration beneath the footing and localized deformation near the footing edges. The deformation pattern indicates localized shear deformation with a general shear failure tendency, although idealized theoretical failure zones were not clearly separated.

3. The manual visual line method estimated orientations of 44.33° and 48.80° on the left and right, respectively. Their arithmetic mean is 46.565° (46.57° to two decimal places); these are approximate image-based orientations, not theoretical slip-surface angles.
4. The two calibrated DEM configurations predicted ultimate bearing capacities of 445.57 kPa for the single-sphere model and 527.87 kPa for the 4-sphere clumped-particle model.
5. The absolute bearing-capacity differences were 20.58% for the single-sphere and 5.91% for the clumped-particle simulation. This indicates closer agreement for the separately calibrated clump configuration in this test; because the calibration and parameters differed, it does not isolate the effect of particle shape.
6. The results are model-scale observations. The reported box and footing dimensions imply potentially restrictive boundary clearance, and the results should not be directly extrapolated to full-scale foundations.

Limitations and future work

The study is limited to one condition: dry, uniformly graded sand. Future work should investigate different gradations, densities, moisture conditions, and particle shapes to evaluate the generality of the conclusions. Repeated tests under identical conditions are also needed to quantify experimental variability.

The narrow model box width introduced boundary confinement, so larger model boxes should be used to evaluate scale effects more rigorously. In DEM, future research should include independent calibration using direct shear or triaxial tests, as well as sensitivity analysis of contact parameters and clump geometry. More objective deformation-orientation extraction methods, such as threshold-based line fitting or strain-field-based approaches, may also be compared with the manual visual line method.

CRediT authorship contribution statement

Mustapha Zakariya'u Lawal: Conceptualization, Methodology, Investigation, Formal analysis, Visualization, Writing - original draft. Kong Fah Tee: Supervision, Conceptualization, Methodology, Writing - review and editing.

Declaration of competing interest

The authors declare that they have no known competing financial interests or personal relationships that could have appeared to influence the work reported in this paper.

Data availability

The data supporting the findings of this study are available from the corresponding author upon reasonable request.

Acknowledgements

The first author acknowledges the support of Beijing Jiaotong University and the China Scholarship Council during his master's research.

References

[1] Bolton MD. The strength and dilatancy of sands. *Géotechnique*. 1986;36(1):65–78. https://doi.org/10.1680/geot.1986.36.1.65

[2] Das BM, Sivakugan N. *Fundamentals of geotechnical engineering*. 5th ed. Boston: Cengage Learning; 2017.

[3] Terzaghi K. *Theoretical soil mechanics*. New York: John Wiley & Sons; 1943. https://doi.org/10.1002/9780470172766

[4] Wood DM. *Geotechnical modelling*. London: Spon Press (CRC Press); 2004.

[5] Janabi FH. *Study of bearing capacity and settlement of footings in silica sands using digital image correlation (DIC)* [thesis]. West Lafayette (IN): Purdue University Graduate School; 2022.

[6] Tong B, Yoo C. Application of digital image correlations (DIC) technique on geotechnical reduced-scale model tests. *Journal of the Korean Geosynthetics Society*. 2022;21(1):33–48.

[7] Cundall PA, Strack ODL. A discrete numerical model for granular assemblies. *Géotechnique*. 1979;29(1):47–65. https://doi.org/10.1680/geot.1979.29.1.47

[8] O'Sullivan C. *Particulate discrete element modelling: A geomechanics perspective*. London: Spon Press (CRC Press); 2011.

[9] Coetzee C, Katterfeld A. Calibration of DEM parameters. In: *Simulations in bulk solids handling: Applications of DEM and other methods*. Weinheim: Wiley-VCH; 2023. p. 1–40.

[10] Cho GC, Dodds J, Santamarina JC. Particle shape effects on packing density, stiffness, and strength: Natural and crushed sands. *Journal of Geotechnical and Geoenvironmental Engineering*. 2006;132(5):591–602. https://doi.org/10.1061/(ASCE)1090-0241(2006)132:5(591)

[11] El Shamy U, Zamani N. Discrete element method simulations of the seismic response of shallow foundations including soil-foundation-structure interaction. *International Journal for Numerical and Analytical Methods in Geomechanics*. 2012;36(10):1303–1329.

[12] Potyondy DO, Cundall PA. A bonded-particle model for rock. *International Journal of Rock Mechanics and Mining Sciences*. 2004;41(8):1329–1364. https://doi.org/10.1016/j.ijrmms.2004.09.011

[13] Zięba Z, et al. Assessing the scale effect on bearing capacity of undrained subsoil: Implications for seismic resilience of shallow foundations. *Materials*. 2023;16(16):5631.

[14] Cerato AB, Lutenegger AJ. Scale effects of shallow foundation bearing capacity on granular material. *Journal of Geotechnical and Geoenvironmental Engineering*. 2007;133(10):1192–1202. https://doi.org/10.1061/(ASCE)1090-0241(2007)133:10(1192)